

Interplays of electron and nuclear motions along CO dissociation trajectory in myoglobin revealed by ultrafast X-rays and quantum dynamics calculations

Megan L. Shelby^{a,1}, Andrew Wildman^b, Dugan Hayes^c, Michael W. Mara^a, Patrick J. Lestrangle^b, Marco Cammarata^d, Lodovico Balducci^d, Maxim Artamonov^a, Henrik T. Lemke^e, Diling Zhu^e, Tamar Seideman^a, Brian M. Hoffman^{a,2}, Xiaosong Li^{b,2}, and Lin X. Chen^{a,c,2}

^aDepartment of Chemistry, Northwestern University, Evanston, IL 60208; ^bDepartment of Chemistry, University of Washington, Seattle, WA 98195; ^cChemical Sciences and Engineering Division, Argonne National Laboratory, Lemont, IL 60437; ^dInstitut de Physique de Rennes, Université de Rennes, 35042 Rennes CEDEX, France; and ^eLinac Coherent Light Source, SLAC National Accelerator Laboratory, Menlo Park, CA 94025

Contributed by Brian M. Hoffman, February 18, 2021 (sent for review December 23, 2020; reviewed by Wojciech Gawelda and Sebastian Westenhoff)

Ultrafast structural dynamics with different spatial and temporal scales were investigated during photodissociation of carbon monoxide (CO) from iron(II)-heme in bovine myoglobin during the first 3 ps following laser excitation. We used simultaneous X-ray transient absorption (XTA) spectroscopy and X-ray transient solution scattering (XSS) at an X-ray free electron laser source with a time resolution of 80 fs. Kinetic traces at different characteristic X-ray energies were collected to give a global picture of the multistep pathway in the photodissociation of CO from heme. In order to extract the reaction coordinates along different directions of the CO departure, XTA data were collected with parallel and perpendicular relative polarizations of the laser pump and X-ray probe pulse to isolate the contributions of electronic spin state transition, bond breaking, and heme macrocycle nuclear relaxation. The time evolution of the iron K-edge X-ray absorption near edge structure (XANES) features along the two major photochemical reaction coordinates, i.e., the iron(II)-CO bond elongation and the heme macrocycle doming relaxation were modeled by time-dependent density functional theory calculations. Combined results from the experiments and computations reveal insight into interplays between the nuclear and electronic structural dynamics along the CO photodissociation trajectory. Time-resolved small-angle X-ray scattering data during the same process are also simultaneously collected, which show that the local CO dissociation causes a protein quake propagating on different spatial and temporal scales. These studies are important for understanding gas transport and protein deligation processes and shed light on the interplay of active site conformational changes and large-scale protein reorganization.

protein structural dynamics | myoglobin | X-ray transient absorption | time-resolved solution X-ray scattering | quantum dynamics calculation

Enzymatic functions frequently involve local motions at the active site as well as large-amplitude motions of the protein, and the two are often strongly correlated. Many chemical processes at the active sites take place as a result of the interplay between atomic movement and electronic structural changes in response to external stimuli such as light, ligand binding, heat or electric field. While reaction kinetics can be predicted from thermodynamic properties, the intrinsic time scales for fundamental chemical events, such as bond breakage and formation, are often unresolved due to challenges in examining rapid electronic and atomic movements in real time. Advanced X-ray sources, especially those with intense photon bursts within the time scale of fundamental chemical events (i.e., femtoseconds), enable structural characterization in terms of the electronic and atomic motions. Combining such ultrashort X-ray pulses with laser excitation, we are able to detect the interplay of ultrafast electron and nuclear motions in the photodissociation of an axial CO ligand from the iron center in the heme site of myoglobin (Mb) (Fig. 1). The same process has been extensively studied due

to numerous functions of heme or other iron porphyrins in hemoproteins, including electron transfer, catalytic oxidation or reduction of metabolites, neutralization of damaging reactive species, and famously the binding of diatomics such as dioxygen, carbon monoxide, and nitric oxide for transportation and sensing (1–6). Because the dissociation of diatomic ligands, such as CO and NO, can be synchronized through optical excitation of the porphyrin, diatomic ligand binding in hemoproteins is amenable to scrutiny by dynamic structural and electronic spectroscopies (1, 7–14). Several X-ray diffraction, solution scattering, and X-ray spectroscopy (including X-ray absorption and emission) studies have been carried out using intense X-ray pulses from synchrotron and X-ray free electron laser sources (11, 14–19). In this report, we focus on the correlations between the electronic structural change of the iron center and these nuclear motions. To investigate these correlations, we used X-ray transient absorption spectroscopy/scattering and theoretical calculations to detect and project detailed trajectories for the CO departure from Fe(II) in the heme site of bovine Mb.

Significance

In this multidisciplinary study, we investigated local and global structural responses upon carbon monoxide (CO) dissociation from the heme iron(II) in myoglobin in solution using ultrafast X-ray absorption and scattering. CO dissociation was optically triggered and pulsed X-rays probed structural and electronic changes as a function of time, revealing an iron(II) spin state transition and nuclear motions propagating from the active site throughout the entire protein. Quantum mechanical computational results were used to assign the iron K-edge absorption features, and to map out electronic and nuclear trajectories during Fe–CO bond elongation and heme macrocycle doming. The study has important implications for heme–protein function and the interaction of small molecule substrates with the metal active centers in enzymes.

Author contributions: M.L.S., D.H., M.C., H.T.L., D.Z., and L.X.C. carried out the X-ray experiments; M.L.S., A.W., P.J.L., M.C., L.B., M.A., X.L., and L.X.C. processed data; M.L.S., A.W., P.J.L., M.C., L.B., M.A., X.L., and L.X.C. analyzed data; and M.L.S., A.W., D.H., M.W.M., M.C., T.S., B.M.H., and L.X.C. wrote the manuscript.

Reviewers: W.G., Universidad Autónoma de Madrid; and S.W., University of Gothenburg.

The authors declare no competing interest.

Published under the [PNAS license](#).

¹Present address: Lawrence Livermore National Laboratory, Livermore, CA 94550.

²To whom correspondence may be addressed. Email: l-chen@northwestern.edu, xsli@uw.edu, or bmh@northwestern.edu.

This article contains supporting information online at <https://www.pnas.org/lookup/suppl/doi:10.1073/pnas.2018966118/-DCSupplemental>.

Published March 29, 2021.

In carbonmonoxymyoglobin (MbCO), the low-spin (LS) Fe(II) center has a pseudo-octahedral coordination geometry, ligated with four nitrogens (N_p) from the heme, the nitrogen of an axial histidine (N_{His} , His93), and CO, a strong field ligand. Previous studies have pointed out that upon excitation of the heme Soret or Q band, photolysis occurs within ~ 50 fs, although there is an ongoing debate about the mechanism of CO photodissociation and the subsequent relaxation of the heme, as well as the possible role of intermediate spin states, similar to those observed in photoexcited iron *Tris*(bipyridine) (20) and ferrous cytochrome *c* (14, 15, 21). With the loss of CO, the LS state of Fe(II) transforms to a high-spin (HS) state and adopts square-pyramidal pentacoordination with the axial histidine His93 moving ~ 0.3 Å out of the porphyrin plane, perturbing the position of the α -helix in which it sits (Fig. 1*B*) (4, 8, 22, 23). Protein control of this movement is critical, both because it is the first step of the mechanism of cooperativity in hemoglobin O_2 binding and because it may lead to a conformational rearrangement of the heme pocket that allows CO to escape and avoid geminate recombination (24).

This CO photodissociation from MbCO, as well as the photolysis of other diatomics such as NO, and the subsequent recombination dynamics have been assessed using X-ray transient absorption (XTA) spectroscopy (Fig. 2) at synchrotron sources with ~ 100 -ps time resolution (19, 25), using Fe K-edge X-ray absorption near edge structure (XANES) spectral features shown in Fig. 2. The main differences between the spectral features of MbCO and Mb are an edge shift to a lower energy and a preedge conversion from two sharp peaks to one broader and weaker peak. These changes are consistent with loss of CO and a conversion of Fe(II) from LS to HS in Mb, as supported by optical and vibrational spectroscopic studies (8, 26).

While heme vibrational cooling was observed by time-resolved Raman techniques on the time scales of a few to tens of ps (26, 27), and optical transient absorption spectroscopy shows the development of broad excited state absorption features with lifetimes of ~ 300 fs and 3 ps, there is an active discussion in the literature as to whether these features can be assigned to an excited-state evolution through a series of electronic intermediate states/species (28–31) or to an exclusively vibrational relaxation pathway (31–33). Because Fe K-edge XTA is sensitive to both the heme iron electronic configuration and the local structural geometry during heme relaxation, measurements of the XANES should distinguish between these mechanisms but only if very fast time scales are resolvable. In this regard, XTA at Linac Coherent Light Source (LCLS) provides a rare opportunity

to investigate these relaxation processes with a technique with both high temporal and structural resolution.

Although the photodissociation of CO from heme and the concomitant LS to HS transition and heme doming motion are well-known phenomena, many fundamental transformations in terms of electronic and nuclear motions that result in the CO departure are not well understood. The recent works on cytochrome *c* and NO-bound myoglobin have made progress in the timing of the spin state transitions on the femtosecond time scale and the identification of the intermediate spin state (14, 15). However, it is far from clear how the spin state change was induced electronically, how the iron spin state is related to the Fe–CO distance, and when the heme doming takes place as the Fe–CO distance elongates in dissociation processes. Understanding these correlations has important implications for other chemical and enzymatic processes involving ligand dissociation. It is therefore of great interest to link dynamic structural and electronic changes at the heme during ligand dissociation to more large-scale conformational changes, especially on the time scale of ligand departure and heme doming, which is expected to take place on tens of femtoseconds to a few picoseconds time scales.

In order to address the dynamic interplay between electronic and nuclear motions that are beyond the Born–Oppenheimer approximation, we carried out combined XTA and X-ray transient scattering measurements during CO photodissociation with sub-100-fs time resolution at the X-ray Pump-Probe (XPP) facility of the LCLS. The kinetics of the spin state transition and the nuclear motion associated with doming, as well as the global motions of the protein matrix, have revealed a series of correlated events as CO departs from the heme. Although the exact trajectory of CO departure in terms of Fe–CO distance and other structural parameters is still difficult to resolve, such processes can be simulated via quantum mechanical calculations to model this process for the Fe(II) center and the ligands directly bound to the metal. The results provide the energetics of different excited states as well as their trajectories as functions of local structural changes, such as Fe–CO distance and heme relaxation, to distinguish the effect of different structural factors on the overall structural dynamics. These calculations also allow us to predict XTA features without and with the structural relaxation of the heme, providing insight into the interplays between the electronic spin state/configuration and corresponding nuclear motions as a function of the Fe–CO distance.

Results and Discussion

The femtosecond XTA measurements that were carried out at the XPP station adopted a beam-multiplexing mode that resulted in a strong dependence of the beam position on monochromator energy; thus, only kinetic traces at selected X-ray photon energies were collected with the laser polarization direction parallel or perpendicular to that of the X-ray (34). The X-ray energies were selected for kinetics trace measurements based on Fe K-edge XANES difference spectra between Mb and MbCO at a 100-ps delay obtained at the Advanced Photon Source, a synchrotron radiation source, as shown in Fig. 2 (19). Guided by this difference XANES spectrum, X-ray photon energy calibration was performed by scanning the incident X-ray energy to maximize the laser-on minus laser-off difference signal at those characteristic energies as labeled in Fig. 2. The energies selected for 3-ps kinetics traces can be divided into preedge, edge, and extended X-ray absorption fine structure (EXAFS) regions, with the first two regions mainly used to extract electronic configurations of the heme iron and the third region used to extract the nuclear movements. Moreover, the global movements of the Mb during the CO photodissociation are further characterized by simultaneous small-angle X-ray scattering measurements with

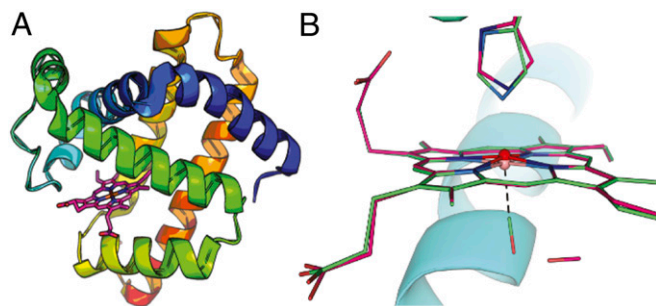


Fig. 1. (A) Mb structure with heme in pink surrounded by helices of the protein. (B) Mb active site structural changes following CO photolysis. Upon photoexcitation, ground state MbCO (green) loses its bond to CO and adopts a square pyramidal structure with His93 (pink), resulting in the doming of the porphyrin where the Fe (red) comes out of the plane of the macrocycle. Structures are from photolysed MbCO trapped at low temperature (12) and ground state (9) MbCO, where their crystal structures are aligned by their respective porphyrin carbons.

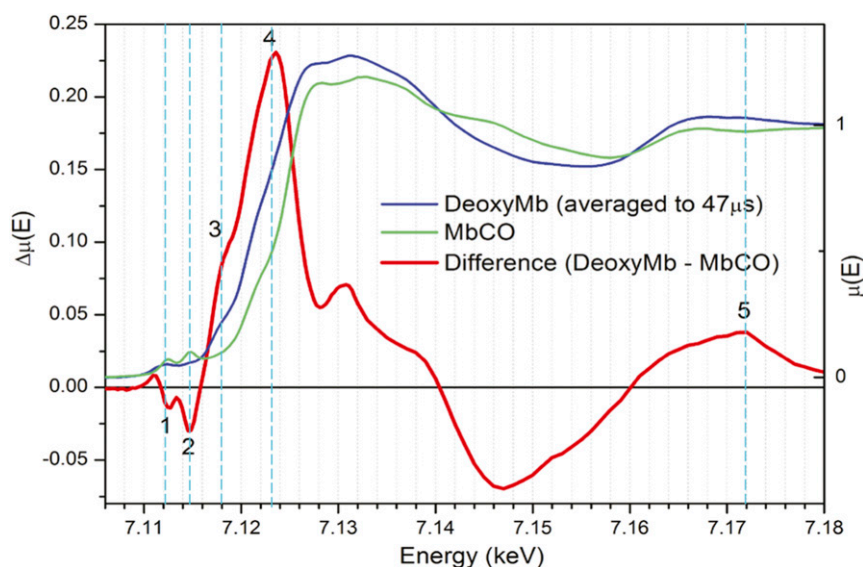


Fig. 2. Fe K-edge XANES and difference spectra measured after CO photodissociation with 100 ps time resolution (19). Energies selected for measurement of polarization-dependent dynamics are marked in dashed vertical cyan lines: line 1, 7.112 keV, the depletion of the ground state transition of $1s \rightarrow 3d_{x^2-y^2}$, $3d_{x^2-y^2}$ character; line 2, 7.115 keV, the disappearance of the preedge peak associated with the CO back bonding antibonding orbital; line 3, 7.118 keV, the rising edge shoulder that appears in MbFe(II); line 4, 7.123 keV, the edge shift; and line 5, 7.172 keV, an EXAFS energy where changes are purely based on changes in the local geometry.

monochromatic X-ray photons within the self-amplified spontaneous emission (SASE) bandwidth.

Structural Dynamics Revealed by Optical Polarization Selected XTA.

Taking advantage of the linear polarization of the laser and X-ray pulses with adjustable relative orientations, optical polarization selected XTA (OPS-XTA) measurements enabled us to probe structural dynamics in an excited state population preferentially aligned with the pump laser polarization. The orientational distribution of the excited state population depends on alignment of the polarization direction of the pump pulse electric field vector \hat{e} with the molecular electronic transition dipole moment $\vec{\mu}$ of randomly oriented molecules in solution, leading to XANES dichroism as different bound state orbitals and absorber-backscatterer directions are probed (*SI Appendix, Fig. S1*). This method is analogous to well-known optical (absorption/emission) anisotropy decay measurements that extract time-dependent electronic transition dipole vector correlation functions, $\langle \vec{\mu}(t) \cdot \vec{\mu}(0) \rangle$, where $\vec{\mu}(t)$ and $\vec{\mu}(0)$ are the optical transition dipole vectors at pump-probe delay times t and 0, respectively (*SI Appendix, Fig. S1*). By selectively probing inner shell transitions along the direction parallel or perpendicular to the valence transition dipole, OPS-XTA introduces another level of sensitivity in electronic structure and local geometry determination to XTA. Sension and coworkers have implemented this approach to resolve the ultrafast structural relaxation of excited vitamin B₁₂ (35–38). Previous studies by Della Longa and colleagues have partially assigned features of the MbCO and Mb XANES based on a combination of electronic structure calculations and both steady state XANES of Mb in solution (18) and through series of polarized XANES of single-crystal MbCO and cryogenically trapped Mb*CO where CO is dissociated but bound elsewhere in the heme pocket (10, 39). For Mb, the overall molecular rotational diffusion time (~ 3 ns) far exceeds the window of our experiments and its effects on the polarization dichroism can be neglected, which simplifies the data analysis compared to optical transient absorption/emission anisotropy of small molecules in solution.

The probability for the ground \rightarrow excited state transition is proportional to $\langle \cos^2(2)\theta \rangle$, where θ is the angle between the polarization direction of the electromagnetic field for the excitation \hat{e} and molecular transition dipole $\vec{\mu}$, and $\langle \rangle$ represents an expectation value calculated from the molecular ensemble. Due to this $\langle \cos^2(2)\theta \rangle$ probability distribution, the excited state molecules will have an initial anisotropic orientational distribution relative to the laser polarization direction. Because the transition dipole of heme Q-band excitation and the general direction of the CO departure are well defined and orthogonal, polarization-dependent XANES signals are expected. The 530-nm laser pump pulse induces a $\pi \rightarrow \pi^*$ transition with the transition dipole in the heme plane to trigger CO photolysis. Therefore, the X-ray absorption signal parallel to the laser polarization direction, s_{\parallel} , is preferentially sensitive to changes in structure and electronic environment that take place in the heme plane, such as Fe–N_p bond elongation that occurs as a consequence of heme core expansion upon occupation of the Fe $3d_{x^2-y^2}$ orbital in the high-spin state. However, the perpendicular polarization signal s_{\perp} contains contributions from both the vectors in the heme plane and normal to the heme plane (*SI Appendix, Fig. S1B*) (defining the heme normal direction as Z and the plane of the heme as the X–Y plane) and thus is more sensitive to the CO departure trajectory.

To isolate axial contributions to the signal, we have adapted a formalism used by Liebisch and Dau to describe steady state X-ray polarization anisotropy in partially ordered samples, as described in *SI Appendix* (40). Analogous to this system, the partially preferred orientation is created in the excited state in our study. This formalism develops an expression for the parallel and perpendicular signals s_{\parallel} and s_{\perp} in the laboratory frame in terms of the contribution to the signal along each molecular axis, c_x , c_y , and c_z . These components of the polarization-dependent absorption signal from each molecular coordinate are averaged over an orientational distribution of excited molecules, which has a probability distribution that depends on the alignment of the molecular axis with the laser polarization direction.

The expression for the component of the signal dependent on heme normal dynamics (c_z) in terms of the parallel and

perpendicular signals, s_{\parallel} and s_{\perp} , is (see derivation of *SI Appendix*, Eq. S11)

$$s_{\perp} - \frac{3}{4}s_{\parallel} = c_z/4 \quad [1]$$

and thus can be extracted from the perpendicular and parallel delay time scans. However, this subtraction significantly compounds the level of noise in these traces, which become very sensitive to noise in the parallel and perpendicular signal. They are plotted with the respective parallel and perpendicular traces at each energy to emphasize the difference between the dynamics for each polarization but are not separately analyzed to obtain kinetics.

Choices of X-ray probe energies, labeled numerically 1 to 5 in Fig. 2, were guided by which features assigned to scattering resonances or electronic transitions had the most relevance to the Mb relaxation mechanism (10, 39, 41). As shown in Fig. 3 C–E, at three energies above the preedge region (7,118, 7,123, and 7,172 eV), perpendicular scans show uniformly faster rises than their corresponding parallel traces. This is consistent with a rapid and dramatic coordination change—likely the dissociation of CO—that occurs along the z axis (19).

The strong positive peak at 7,123 eV in the difference spectrum (Fig. 2, labeled 4) is an indication of a down-shift of the K-edge energy originating from several factors: 1) an increase in overall electron density centered on iron, which is greater in Mb than in MbCO because of the loss of the backbonding between the CO ($2p_x$ and $2p_y$) and Fe ($3d_{xz}$ and $3d_{yz}$) orbitals; 2) the lowering of the energy of the $4p_z$ orbitals due to the Fe(II) coordination geometry change from hexacoordination to penta-coordination (10, 39); and 3) the increase in the average Fe–N bond length, which increases the EXAFS oscillatory frequency and thus shifts the edge position down in energy (42). These

effects are often invoked to explain ligation or deligation induced edge shifts in hemes that have nominally unchanged formal charge (25, 43). The down-shift of the Fe K-edge position, monitored at 7,123 and 7,118 eV, mostly appears very rapidly (<100 fs), and this rapid growth accounts for the majority of the XANES difference at these energies. The perpendicular polarization is more sensitive to this fast phase, suggesting that the initial edge shift cannot be solely attributed to the expansion of the Fe–N_p bonds as CO dissociates and the heme core expands. The signal intensities at parallel and perpendicular polarizations at 7,123 eV differ even after several picoseconds, indicating that the edge shift is more dependent on heme normal contributions even after the initial structural relaxation shown by the heme normal signal c_z decay in about 500 fs (Fig. 3D). Thus, there are slower processes in the heme plane that lead to depolarization on a few picosecond time scale. These results demonstrate the validity of the X-ray absorption anisotropy or OPS-XTA, which will be explored in more systems in the future.

Well above the absorption edge but on the low-energy end of the EXAFS region at 7,172 eV, contributions from single scattering events sensitive to local geometry, such as the nearest neighbor distances, dominate. The broad positive feature centered at 7,172 eV in the 100-ps difference spectrum is indicative of a shift in the sum of the EXAFS oscillations, both due to the loss of an axial ligand and to the shift of the oscillation associated with the Fe–N scattering to higher frequency as the bond length increases. The perpendicular polarized scans at 7,172 eV (Fig. 3E) also exhibit a fast rise followed by a slower increase in the difference signal. Because this energy is mostly dependent on the number of ligands directly coordinating Fe and their relative bond lengths, we can interpret this sharp rise as directly due to the loss of CO as an axial ligand. The parallel polarization has less of this sharp rise and evolves more slowly within the first

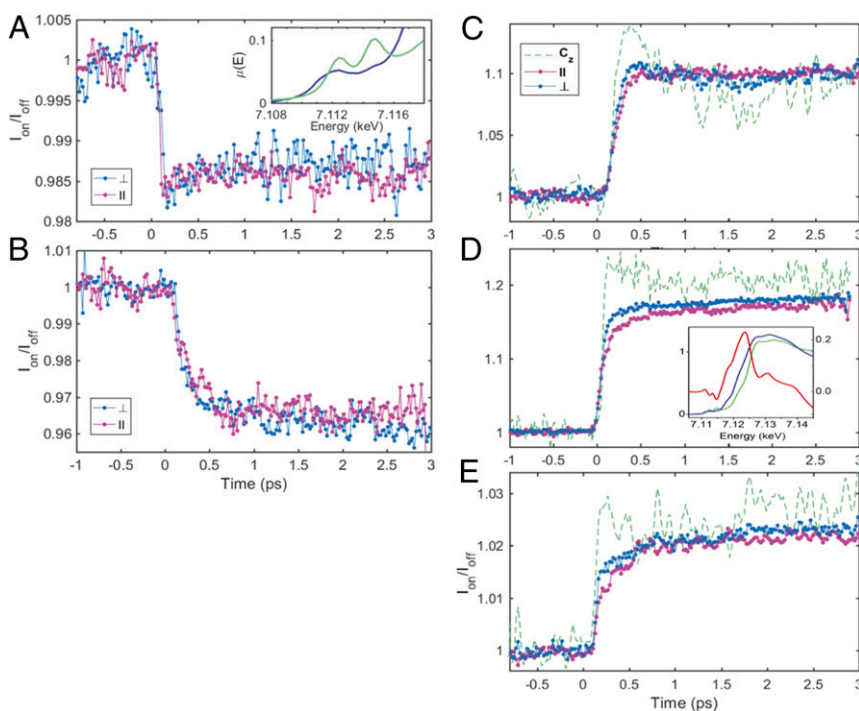


Fig. 3. Averaged time delay scans at (A) 7,112, (B) 7,115, (C) 7,118, (D) 7,123, and (E) 7,172 eV (corresponding to the energies labeled 1 to 5 in Fig. 2) for the parallel polarization, perpendicular polarization, and (for C–E) the z component of the signal, c_z . The numbers in parentheses are energy labels in Fig. 2. Data are normalized by the ground state signal intensity measured by laser drop shots throughout the scan and are represented as $I_{\text{on}}/I_{\text{off}}$. A, Inset, shows the preedge features at 7,112 and 7,115 eV, and D, Inset, shows difference XANES features at 7,118, 7,123, and 7,172 eV where the kinetics traces were collected, respectively.

picosecond. These results provide the time scales for the nuclear motions, largely those in heme, due to the CO departure.

A feature that appears at 7,118 eV in the transition edge shown in the difference spectrum (Fig. 2) was found to be polarized normal to the heme plane in polarized single-crystal experiments (39). DFT calculations of ground state Mb Fe K-edge transitions below and near the rising edge identify this feature as consisting mostly of the Fe $4p_z$ orbital hybridized with various orbitals of the His nitrogen (18). In the delay time scans at 7,118 eV, this component grows in within 100 fs and for perpendicular scans reaches a maximum at ~ 400 fs and slightly decays within about 1 ps (Fig. 3C). The corresponding plot of c_z reflects the relative decay of the heme-normal contribution to the perpendicular difference signal as it dips below the parallel difference signal. These become apparent in the section below.

Dynamic Electronic and Nuclear Trajectories Revealed by the Preedge Features. The iron K-edge preedge features in the 7,106- to 7,117-eV region are from quadrupole-allowed $1s \rightarrow 3d$ transitions that gain dipole character from $3d/4p$ mixing (18, 19). Although these features are weak, they provide fingerprint information on vacant iron molecular orbitals (MOs), coordination geometry, 3d electronic configuration, and oxidation state (44), complementary to the occupied orbital configuration obtained from X-ray emission spectroscopy (XES) (14, 15). There are two distinct preedge peaks at 7,112 and 7,115 eV (Fig. 2, labeled 1 and 2, respectively) in the LS Fe(II) in MbCO. To assist in peak assignment, DFT modeling of the ground state MbCO Fe K-edge XANES transitions was carried out (see *SI Appendix* for details of theoretical calculations). From these calculations, the 7,112-eV peak is assigned to a set of combined transitions with mostly $1s \rightarrow 3d_{z^2}$ and $1s \rightarrow 3d_{x^2-y^2}$ character with significant hybridization with the $4p$ orbitals. These transitions move electron density into the antibonding σ orbitals of the Fe-C ($[3d_{z^2} + \sigma(\text{CO})]^*$) and the Fe-N_p ($[3d_{x^2-y^2} + \pi_{\text{porph}}]^*$) bonds, respectively. The 7,115-eV peak is due to the transition from $1s$ to $3d$ MO vacated from electron donation from the occupied Fe $3d_{xz}$ and $3d_{yz}$ MOs to the π antibonding orbital of CO (*SI Appendix*, Fig. S3).

When the strong field ligand CO departs from Fe(II), these two preedge peak intensities collapse as a result of the Fe(II) LS to HS state transition, which significantly reduces 10Dq and increases the number of $1s$ to vacant $3d$ MO transitions. The kinetic trace at the 7,112-eV feature has an almost instantaneous depletion upon photoexcitation, followed essentially by a plateau throughout the remainder of the 3-ps delay time window without any detectable excitation polarization dependence (Fig. 3A). This result confirms the assignment of this preedge feature to mostly $1s \rightarrow 3d_{z^2}$ and $1s \rightarrow 3d_{x^2-y^2}$ character, which extends the electron density change in both parallel and perpendicular directions with respect to the transition dipole in the heme macrocycle plane. In other words, the processes that have the most impact on the magnitude of this feature at 7,112 eV all occur within 100 fs, including 1) the loss of CO, 2) the LS to HS [or an intermediate spin state (14, 15)] state transition of Fe(II), 3) a reduction of the ligand field energy splitting, and 4) changes in the $3d$ - $4p$ mixing. In contrast, the kinetics at the 7,115-eV peak, whose intensity is also influenced by the loss of back-bonding, show a much slower depletion with a time constant of ~ 300 fs (Fig. 3B).

The significant difference in the kinetics of the two preedge peak depletions seems to contradict their assignments above since both the Fe-C σ bond ($[3d_{z^2} + \sigma(\text{CO})]^*$) and the Fe-N_p σ bonds ($[3d_{x^2-y^2} + \pi_{\text{porph}}]^*$), as well as the $3d$ back bonding from CO, should all diminish within the rapid CO dissociation time, irrespective of other geometric or electronic changes. In order to decipher this apparent disagreement, the energy-specific time-dependent density functional theory (ES-TDDFT) (6, 7) method

was used to calculate electronic and nuclear structural changes of the Fe(II) in heme and the corresponding XANES spectral evolution as a function of the Fe-CO distance, mimicking photoexcitation and subsequent CO departure trajectories, including changes in the Fe(II) spin state, $3d$ electron occupation, and the heme macrocycle structural relaxation. In particular, we tracked the energy evolution of the Fe(II) spin state as a function of the Fe-CO distance and identification of specific structural influences on the transient XANES features by major reaction coordinates along the CO dissociation pathway, namely, the Fe-CO distance and heme doming. An energy minimized structure was used for the ES-TDDFT calculations in which His93 and CO are axial ligands of Fe(II) in the heme, but the influence of the remaining protein is neglected. Due to this model, these results show a trend of energy variations rather than absolute and accurate values but capture the necessary physics to characterize the XANES spectrum. These calculations identified possible electronic states participating in the relaxation pathway that were consistent with previous computational efforts (45) to describe the energy landscape associated with CO dissociation. To determine the Fe(II)-CO bond length that enables the Fe(II) LS to HS transition, the energies for various valence excited states of different spin multiplicities were calculated as a function of Fe(II)-CO distance and plotted in Fig. 4 (see computational details in *SI Appendix*).

Relaxed geometries for several states of interest, specifically $(3)(xz, z^2)$ and the HS quintet state, were computed, and results are tabulated in Table 1.

As the Fe-CO distance increases, the energy for the LS state becomes destabilized, while that for the HS quintet state is almost unchanged but is at a much lower energy than the initially populated π - π^* state by the photoexcitation and those of the possible (1, 3) MLCT (metal-to-ligand-charge-transfer) states. Interestingly, the triplet energy stabilizes at Fe-CO distance of 2.5 Å, at which its energy is closest to that of the HS quintet state. Thus, the fastest time constant is the estimated upper limit and faster processes are likely. However, our experimental time resolution was still insufficient to clearly identify the exact trajectory because the CO departure time is much shorter than 100 fs. Calculation of the XANES features was also carried out for

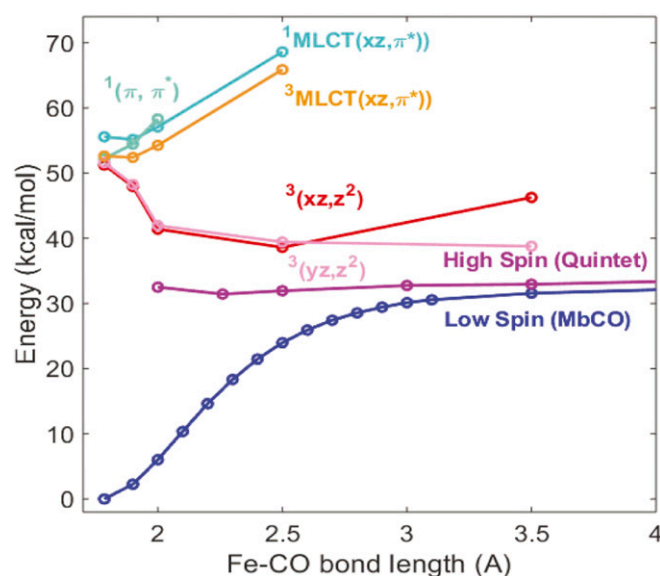


Fig. 4. Energy relative to the relaxed ground state MbCO vs. Fe-CO distance for likely electronic state participants in Mb relaxation pathway. The dominant character of each state is indicated in the same color as their respective energy lines.

Table 1. Relaxed geometries of excited states identified by TDDFT

| Distance (Å) | MbCO | Relaxed $^3(xz, z^2)$ | Relaxed quintet |
|-------------------|------|-----------------------|-----------------|
| Fe-N (Heme) | 2.06 | 2.05 | 2.13 |
| Fe-N (His) | 2.05 | 2.19 | 2.15 |
| Fe-C _α | 3.12 | 3.13 | 3.19 |
| Fe-C _m | 3.52 | 3.52 | 3.55 |
| Fe-C _β | 4.40 | 4.40 | 4.46 |
| Fe doming | 0.05 | −0.09 | −0.30 |

inner shell transitions from 1s to higher energy orbitals in the Fe K-edge XANES region in both the LS state in MbCO and the HS state in Mb. The calculated XANES features give rather good agreement with the experimental observations, reproducing the two preedge peaks at 7,112 and 7,115 eV in the starting MbCO state and the collapse of the higher-energy peak as well as red-shift of the lower-energy peak on CO dissociation (see Fig. 5 *A* and *B*). In recent ultrafast XES studies, Chergui and coworkers identified an intermediate iron triplet spin state in myoglobin-NO and cytochrome *c* ligand photodissociation with approximately a 600-fs lifetime (14, 15), which is not resolved here since the energy shift difference is beyond the experimental resolution.

Although our experimental time resolution was insufficient to follow the CO dissociation in real time in <100 fs, the spectral evolution in the XANES region along the CO departure trajectory can be captured with calculations of the Fe K-edge bound transitions along the dissociation coordinate. Fe K-edge transitions were calculated with the Fe–CO distance varying from 1.79 (from the relaxed MbCO geometry) to 2.40 Å. These transitions were calculated both with and without geometric relaxation of the heme at each point along the Fe–CO bond elongation trajectory, as seen in Fig. 5C. The intensities of the two preedge peaks first decrease as the Fe–CO bond stretches to about 2.2 Å, and then a single peak at about 7,111.2 eV starts to emerge as the Fe–CO distance grows to 2.4 Å. Such a spectral evolution can be explained by the coordination symmetry changes that enable different d–p mixing along the trajectory. At short Fe–CO distances, the stronger Fe–CO bonding compared to the Fe–N_{His} causes an asymmetry along the *z* axis (*SI Appendix*, Fig. S1) to enable some amount of d–p mixing. As the Fe–CO distance starts to increase, the Fe–CO bond weakens and thus symmetrizes the ligands along the *z* axis, making the Fe(II) site more centrosymmetric and reducing d–p mixing to result in a decrease of the preedge intensities. As Fe(II)–CO distance becomes even longer, approaching pentacoordinated Fe(II), the asymmetry along the *z* axis and hence the d–p mixing increase again, resulting in an increase in the peak intensity. These results describe the convolutions of the preedge feature evolution as both the nuclear structure and electronic spin change within a time window of ~100 fs. Nevertheless, this does not explain the difference in the kinetics observed at the two preedge peaks, which turns out to be related to the spectral evolution in the electronic transitions along the rising edge as discussed below.

Influence of Higher-Energy Electronic Transitions on the Observed Kinetics at the Preedge. As we examine the spectral evolution shown in Fig. 5C, the rise of intensities for the transitions above 7,116 eV with increasing Fe–CO distance is significant. In order to distinguish electronic and nuclear structural effects during the CO dissociation, XANES spectral features were calculated for the excited triplet and quintet states in three constrained structures: structure **a**, the ground state structure, assuming the heme is still frozen after the CO departure; structure **b**, a relaxed heme with a fixed Fe–N_{His} distance to exemplify the doming motion

only; and structure **c**, a fully relaxed heme and axial histidine to include both doming and Fe–N_{His} distance elongation (Fig. 6). Structure **a** results in a set of transitions at ~7,116 eV, while structures **b** and **c** result in features further shifted to ~7,117 eV. Allowing His93 to move away from the Fe (structure **c**) also increases the intensity in this region.

The polarization-dependent XANES spectra were also calculated for the triplet and quintet states to aid interpretation of heme normal polarized dynamics at 7,118 eV (*SI Appendix*, Fig. S2). To capture the polarization-dependent spectra, the oscillator strength for each transition was calculated for each Cartesian component of the transition dipole, rather than the isotropic average. For both the triplet and quintet electronic states, the primarily heme normal polarized transitions for the structure **a** with the ground state geometry appear at 7,116 eV (*SI Appendix*, Fig. S2). The structure **b** allowing the heme to relax but keeping the Fe–N_{His} bond length fixed at the ground state value causes a blue shift in this peak. When the Fe–N_{His} bond length is allowed to relax (structure **c**), the energy of these transitions is relatively unaffected, but the oscillator strength is higher than that of the structure **b** due to the elongation of the Fe–N_{His} bond in the heme doming motion that leads to greater orbital mixing with the histidine ligand.

Notably, the rise of new features around 7,118 eV from the less constrained structures **b** and **c** are rather broad, with their tails extending into the 7,115 eV region. The instantaneous rise and slower decay of this component (Fig. 3 *A* and *B*) compensates for the depletion of the 7,115-eV peak intensity discussed earlier and results in an apparent retardation of the signal depletion kinetics compared to those at 7,112 eV, even though both signals are directly related to CO departure. Therefore, this result agrees with those from ultrafast optical and vibrational spectroscopies in that the departure of CO occurs in less than 100 fs, and while some component of the decay of this feature is rapid, there are also large contributions from slower dynamics involving the heme ring motion as discussed later (*vide infra*). Previous DFT calculations by Lima et al. suggest that the feature around 7,118 eV in Mb is due to a mixing of a large number of orbitals or surrounding residues with the Fe 4p_z characters (18). Our calculations show significant metal 4p_z character in the relevant MO, which is distributed above and below the heme macrocycle plane and delocalized over the macrocycle itself, as shown in *SI Appendix*, Fig. S2C. Such results suggest that the transitions around 7,118 eV should be sensitive to both the Fe–N_{His} bond length and ring conformation changes such as Fe(II) doming, which may alter the MO mixing and energies. Therefore, the electronic spin state transition and geometry change together are attributed to the different kinetics at the two preedge features.

Photodissociation Reaction Trajectory Extracted from Global Fitting of XANES Difference Signals. To better determine the distinct relaxation processes detected in the time evolution of the OPS-XTA signals at each characteristic energy, kinetics signals at both parallel and perpendicular relative polarizations were globally fit to a sequential kinetics model as described below and in *SI Appendix*, *Methods*, section S5 (n.b. the kinetics trace at 7,112 eV was excluded from the global fit due to its weak signal). The vast majority of pump probe studies of CO photolysis in Mb are consistent with a three- or four-step sequential process beginning with the (π , π^*) Franck Condon state (*S*₁) and ending with the partially relaxed HS Fe(II) state (*Mb*_{HS}). Full vibrational relaxation of the heme is thought to occur within 15 to 20 ps (26, 27, 32). Here we only focus on kinetic processes within the first few picoseconds.

A three-step sequential model was minimally required for a global fit of the kinetics data (described in *SI Appendix*):

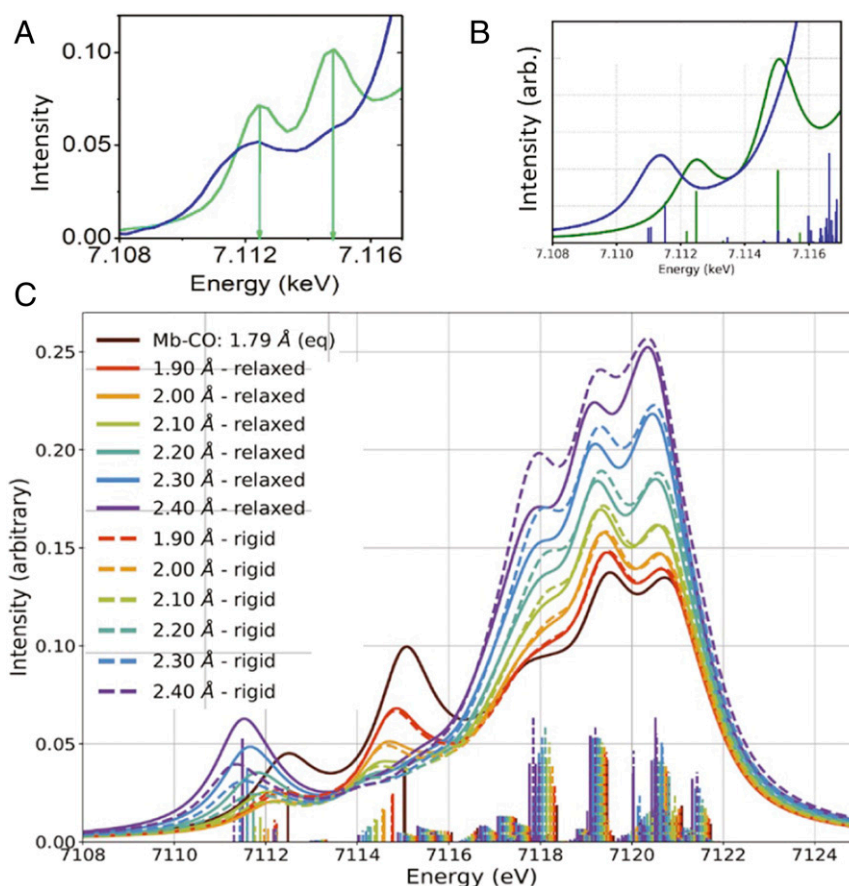
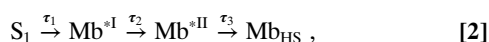


Fig. 5. Preedge features (A) measured at APS at 0 (blue) and 100 ps (green) and (B) calculated for LS MbFe(II)CO (blue) and HS MbFe(II) after CO dissociation (green) that shows qualitative agreement with A. (C) The calculated XANES features in the preedge region as a function of Fe–CO distance from 1.79 to 2.40 Å as marked in the legends with (solid lines) and without (dashed lines) the macrocycle structural relaxation. In either condition, the double preedge peak (brown) evolves into a largely single peak (purple) reflecting the noncentrosymmetry from large to small and large again as described in *Dynamic Electronic and Nuclear Trajectories Revealed by the Preedge Features*.



where Mb^{*I} and Mb^{*II} are intermediate species or populations. Simulated traces were calculated based on numerical integration of the differential rate expression describing the rate of change of each population in the kinetics scheme and iteratively fit at all energies. The total difference in XAS absorption is expressed as a function of the X-ray photon energy E and the pump–probe delay time t at each energy,

$$\Delta A_{total}(E, t) = \sum_{i=0}^n \Delta A_i(E) P_i(t), \quad [3]$$

where i is the index of the states, corresponding to Mb^{*I} , Mb^{*II} , and Mb_{HS} ; $\Delta A_i(E)$ is the relative change in absorption of the i th state at E ; and $P_i(t)$ is the population of i th state at t and convoluted with a Gaussian instrument response function to compute each simulated trace. Three time constants and three species or populations were required to adequately fit the data as represented in the above kinetics scheme, where $\tau_1 = 0.08 \pm 0.01$ ps, $\tau_2 = 0.89 \pm 0.12$ ps, and $\tau_3 = 3.46 \pm 2.01$ ps. The instrument response function obtained from the global fit was 0.07 ± 0.01 ps, close to the estimate of 0.08 ps. Thus, the shortest time constant τ_1 is an upper limit, while faster processes are likely. Because we only sample the first 3 ps after excitation, the largest, 3.46 ps, time constant is at the limit of what is resolvable under our experimental conditions, but fits invariably fail without the

inclusion of such a long time constant. These time constants are in line with the published work on cytochrome *c* and Mb–NO, which are similar but not identical systems (14, 15).

What distinguishes this study from the previous ones are the fits for the parallel and perpendicular kinetic traces at 7,123 eV, shown in Fig. 7A as an illustrative example, and the individual contributions from the Mb^{*I} , Mb^{*II} , and Mb_{HS} states to the difference signal obtained from the fit, shown in Fig. 7B. Values of ΔA for each component are collected in Table 2. Because the S_1 state originating from the π to π^* transition in the macrocycle has very similar Fe(II) electronic and geometric structures as the ground state, it is expected to have a negligibly small ΔA , and it is not included in the fits.

For all energies, the magnitudes of $\Delta A(Mb^{*I})$ and $\Delta A(Mb_{HS})$ are larger in the perpendicular polarization than in the parallel polarization, while the opposite is true for $\Delta A(Mb^{*II})$. Furthermore, with the exception of the perpendicular polarization at 7,118 eV, the magnitude of $\Delta A(Mb^{*I})$ is uniformly less than that of $\Delta A(Mb^{*II})$, especially in the parallel polarization. We also find that the magnitude of $\Delta A(Mb^{*II})$ in either polarization is smaller than $\Delta A(Mb_{HS})_{\perp}$, while $\Delta A(Mb_{HS})_{\parallel}$ is smaller than or about the same magnitude as $\Delta A(Mb^{*II})_{\parallel}$. Utilizing the time constants and ΔA values obtained from the global fit, observations at individual energies, and XANES modeling of identified excited states, Mb^{*I} and Mb^{*II} can be assigned.

The heme plane polarized nature of Mb^{*II} is compelling evidence that the appearance of this species is due to Fe–N_p bond

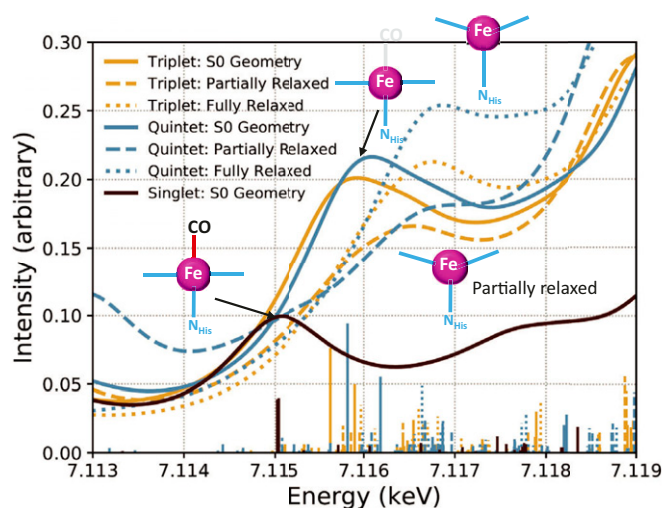


Fig. 6. Calculated XANES transitions for the higher-energy preedge peak at 7.115 keV of ground state (black), triplet state (dark yellow), and quintet state (blue) with the ground state structure (solid lines) fixed Fe–N_{His} distance and relaxed heme macrocycle (dashed lines) and fully relaxed structure (dotted lines). As CO departs, new absorption features emerge at 7.116 keV which partially cancelled out the intensity depletion resulting from the CO departure at 7.115 keV, making the apparent retardation of the kinetics at 7.115 keV.

elongation. While some doming occurs in the relaxed triplet geometry, the relaxed quintet geometry shows a complete 0.07-Å expansion of all four Fe–N_{Heme} bonds. The 800-fs time constant is therefore assigned to the formation of the quintet state and accounts for this structural relaxation process. The XANES reflect the effects of Fe–N_p elongation, which contributes further

Table 2. Fitted values of ΔA for Mb^{*I}, Mb^{*II}, and Mb_{HS} vs. energy and polarization

| Energy (eV) | ΔA_{\perp} | | | ΔA_{\parallel} | | |
|-------------|--------------------|-------------------|------------------|------------------------|-------------------|------------------|
| | Mb ^{*I} | Mb ^{*II} | Mb _{HS} | Mb ^{*I} | Mb ^{*II} | Mb _{HS} |
| 7,115 | −0.026 | −0.033 | −0.037 | −0.023 | −0.036 | −0.020 |
| 7,118 | 0.10 | 0.07 | 0.11 | 0.083 | 0.090 | 0.085 |
| 7,123 | 0.14 | 0.15 | 0.18 | 0.12 | 0.15 | 0.16 |
| 7,172 | 0.015 | 0.020 | 0.022 | 0.012 | 0.022 | 0.015 |

to the edge shift and lends a slow rise to the dynamics at 7,172 eV. This also explains the trend of larger values of ΔA for Mb^{*II} compared to Mb^{*I} as these changes positively compound with the difference signal that arises from the formation of Mb^{*I}. Calculated XANES of the relaxed quintet clearly show an increased in-plane contribution compared to the quintet XANES calculated at the S₀ geometry, while the triplet state XANES has no such additional in-plane contribution upon relaxation (*SI Appendix, Fig. S2*). The ~3-ps rise of Mb_{HS} can be ascribed to some component of the vibrational relaxation of the heme. Picosecond resonance Raman studies find a similar time constant (~3 ps) for the relaxation of high-frequency in-plane modes of heme.

A recent ultrafast small-angle scattering study by Levantino and Cammarata showed that the force exerted on the F helix where the axial histidine of Mb is bound causes the helix to move with a time constant of 400 fs (17, 46). This provides a limit on the Fe–N_{His} bond expansion time following CO dissociation, which must occur prior to F helix movement, and is consistent with the assignment of the 80-fs time constant to the generation of the (xz/yz, z²) triplet as this state exhibits a 0.14 Å Fe–N_{His} bond length expansion and a −0.09 Å movement of Fe out of the porphyrin plane in the relaxed geometry.

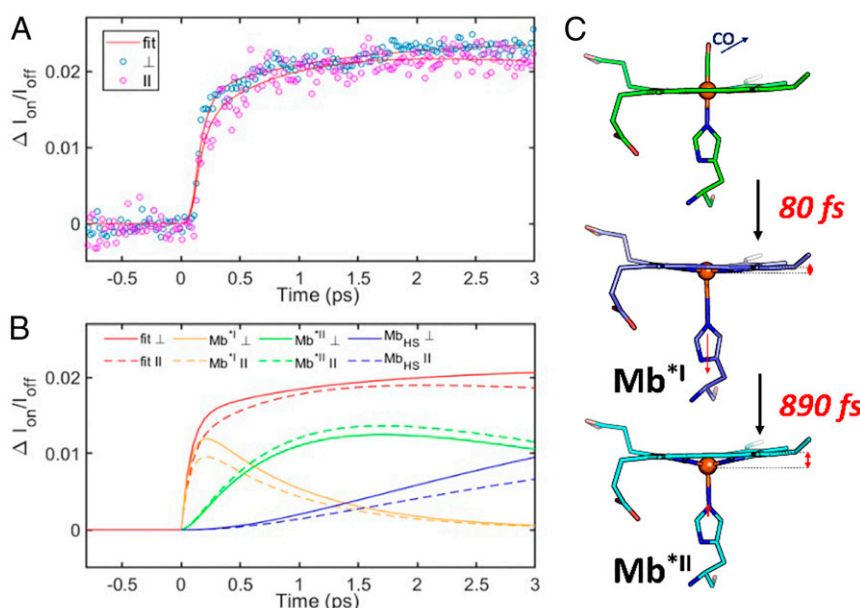


Fig. 7. (A) Global fits to a three-step sequential model for both polarizations at (4) 7,123 eV. (B) Components of the fits from each species for the perpendicular (solid) and parallel (dashed) polarizations. (C) Proposed mechanism of heme relaxation following photodissociation of CO. The 80-fs component is attributable to CO loss, intersystem crossing, a small displacement of Fe out of heme plane, and elongation of Fe–N_{His} bond. The 890-fs component is due to the expansion of Fe–N_p bonds, heme doming, and further Fe out-of-plane displacement.

Global Protein Motions Triggered by CO Photodissociation from Heme Fe. Because the motions in proteins span multiple temporal and spatial scales, the X-ray solution scattering data were acquired simultaneously with the XTA data using a 2D pixelated detector (CSPAD) collecting forward scattering radiation using the monochromatic X-ray beam. The simultaneous data collection provides a full picture of the dynamics, from the localized photodissociation to the propagation of the mechanical relaxation, with no uncertainty with respect to potential differences in excitation fluence or temporal overlap. It also provides the opportunity to observe anisotropy in both the X-ray absorption and scattering data. Although most previous ultrafast protein scattering measurements have been carried out using the full SASE bandwidth available at the LCLS, our measurements were carried out using monochromatized X-rays. These results therefore demonstrate the feasibility of simultaneous data acquisition in such a combined experimental approach.

The details of the measurements have been described previously by Levantino et al. (17, 46). The time resolved scattering data in a Q range of 0.01 to 3 \AA^{-1} are displayed in Fig. 8A. Here we only focus on the low Q region, $Q = 0.02$ to 0.26 \AA^{-1} , corresponding to lengths ranging from 2.4 to 30 nm. The negative signals indicate an overall decrease of the electron density in this length range, due to the volume increase of the protein as CO departs from the heme. The higher Q range data will be analyzed in future studies with extensive analysis and modeling that are beyond the scope of this report. A polarization analysis has been attempted, but the signal to noise ratio did not allow the retrieval of polarization dependence as suggested in the literature (16).

The small-angle data were analyzed in terms of change of radius of gyration and volume as done in a previous study (17). By further dividing the Q range 0.02 to 0.26 \AA^{-1} into 0.02 \AA^{-1} intervals, we show in Fig. 8B plots of the inverted averaged signals in each interval as a function of the probe delay time from

the laser excitation that triggers the CO departure. As previously observed (17), the scattering signals in this Q region oscillate with time after the perturbation of CO photodissociation from heme. A two-step process is observed. Initially, the radius of gyration changes without significant change of the protein volume. This can only be explained by a mass redistribution inside the protein with mass moving outward as result of bond photolysis. Such stress needs time to reach the surface (~ 1 ps), driving transient protein expansion. Interestingly, the ~ 1 -ps time scale is quite similar to the heme structural relaxation of detected by X-ray absorption spectroscopy described earlier.

Such a volume expansion on different time scales throughout the protein illustrates a protein quake in real time. Fig. 8C and D depict changes in the radius of gyration ΔR_g and the volume ΔV , which indicate that these changes can take place in ~ 1 ps. Interestingly, the onset of ΔV has about 1 ps delay from that of ΔR_g if the values are extracted from the total small-angle signals in the q region of 0.05 to 0.2 \AA^{-1} . These results are in an agreement with kinetics time constants of τ_2 of 0.9 ps, and τ_3 of 3.5 ps extracted from the XTA data described above, corresponding to the protein matrix responses to the step-wise structural relaxation from the heme site. The combined results from XTA and XSS provide a dynamic map for accurate time scale and spatial scale for the propagation of structural dynamics from heme perturbation through the protein matrix, which could guide us in understanding enzyme actions in many other systems. As an alternative interpretation of the XSS signals, Brinkmann and Hub have performed extensive MD simulations to propose that the protein quake signals instead arise due to the mainly the hydration solvent shell dynamics (47), definitively proving the validity of either model will be beyond the current work and will be inspiring motivation for the future work.

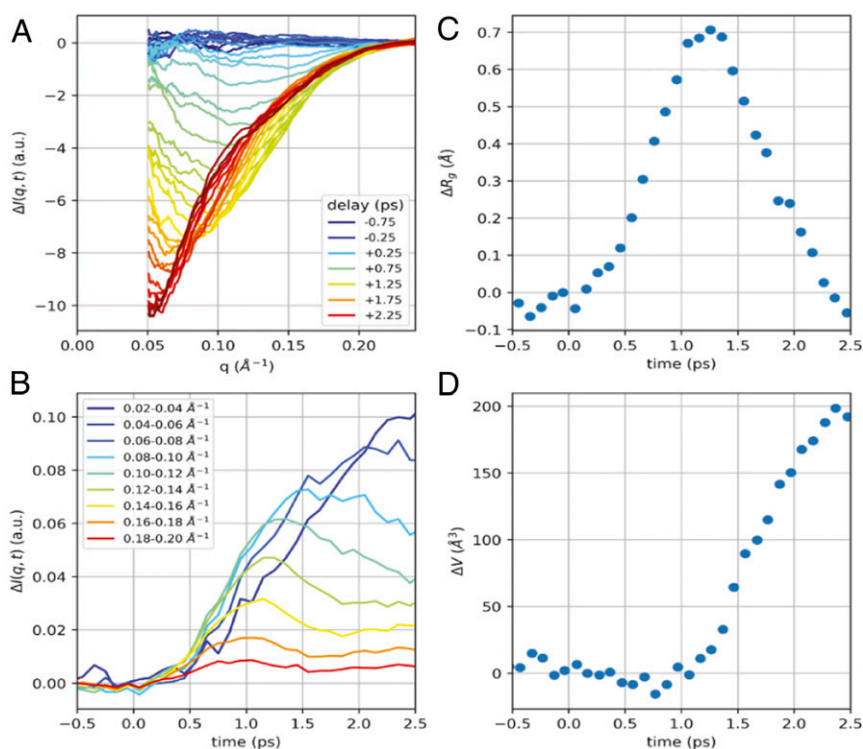


Fig. 8. (A) X-ray transient scattering signals simultaneously collected as the X-ray transient absorption measurements in the time window of ~ 3 ps and displayed here in a Q range from 0.05 to 0.2 \AA^{-1} . (B) Signal intensities at different Q intervals as shown in the legends as a function of the pump-probe delay time. (C) ΔR_g (radius of gyration change) vs. delay time. (D) ΔV (volume change) vs. delay time.

Summary

The electronic and nuclear dynamics following CO photodissociation from heme in myoglobin were investigated using a combination of simultaneous ultrafast X-ray transient absorption, X-ray transient scattering measurements, and computational studies. The optical polarization selected-XAS measurements, in combination with TDDFT calculations, successfully elucidate the CO departure trajectory as well as the intricate spin dynamics as the Fe transition from the low- to high-spin states. Our results demonstrate that the rapid formation of a ($xz/yz, z^2$) triplet state occurs with a time constant of 80 fs as CO dissociates, accompanied by the elongation of the Fe–N_{HIS} bond. The calculations confirm our spectral assignments for the preedge features, distinguishing the different relaxation steps (partial to full structural relaxation) and their corresponding XTA features. The combined approach enables the interpretations of apparent kinetics difference at the two preedge features as the emergence of new spectral features derived from structural changes in the triplet and quintet intermediate states. The X-ray scattering data, measured simultaneously with X-ray absorption, reveal the onset of volume expansion due to the CO photodissociation, a protein quake propagating from local to global length scales of the protein, in good agreement with the kinetics results from X-ray absorption. Expansion of the Fe–N_p bonds occurs with the subsequent formation of the quintet state with a time constant of 0.89 ps, which causes protein matrix expansion in a range of ~24 to 35 Å from the epicenter. These studies demonstrate the

interplay between active site and protein bulk dynamics and are essential for understanding protein ligand photolysis and gas transport properties in physiological systems.

Data Availability. All study data are included in the article and [SI Appendix](#).

ACKNOWLEDGMENTS. We acknowledge support for this work from the Ultrafast Initiative (theoretical work) of the US Department of Energy (DOE), Office of Science, Office of Basic Energy Sciences, through Argonne National Laboratory under contract DE-AC02-06CH11357, and M.L.S. is supported by the NIH under contracts R01-GM115761 (L.X.C.) and R01-HL63203 (B.M.H.). Use of the LCLS, SLAC National Accelerator Laboratory, is supported by the US DOE, Office of Science, Office of Basic Energy Sciences under contract DE-AC02-76SF00515. Computations on modeled spectra were facilitated through a DOE Computational and Theoretical Chemistry grant (DE-SC0006863 to X.L.) and the use of advanced computational, storage, and networking infrastructure provided by the Hyak supercomputer system at the University of Washington, funded by the Student Technology Fee. P.J.L. is also grateful for support from the state of Washington through the University of Washington Clean Energy Institute. M.L.S. also thanks the National Institute of General Medical Sciences of NIH for support through the Molecular Biophysics training grant administered by Northwestern University (5T32 GM008382) to L.X.C. and through Grant 5R01GM111097 to B.M.H. T.S. is grateful to the US DOE, Atomic, Molecular Optical Science Program, Grant DE-FG02-04ER15612/0013. D.H. acknowledges support from the Joseph J. Katz Fellowship from Argonne National Laboratory. M.C. and L.B. acknowledge CNRS [Projets Exploratoires Premier Soutien Soutien aux Activités Scientifiques Françaises autour des Lasers à Électrons Libres Émettant des Rayons X (PEPS SASLELX)] and the support of European Union Horizon2020 under the Marie Skłodowska-Curie Project X-Probe Grant 637295.

1. H. Frauenfelder, B. H. McMahon, P. W. Fenimore, Myoglobin: The hydrogen atom of biology and a paradigm of complexity. *Proc. Natl. Acad. Sci. U.S.A.* **100**, 8615–8617 (2003).
2. K. M. Kadish, K. M. Smith, R. Guilard, *The Porphyrin Handbook* (Academic Press, New York, 1999).
3. Y. Huang *et al.*, Photolysis of the histidine-heme-carbon monoxide complex. *J. Am. Chem. Soc.* **113**, 9141–9144 (1991).
4. R. Patra, A. Chaudhary, S. K. Ghosh, S. P. Rath, Axial ligand orientations in a distorted porphyrin macrocycle: Synthesis, structure, and properties of low-spin bis(imidazole) iron(III) and iron(II) porphyrins. *Inorg. Chem.* **49**, 2057–2067 (2010).
5. W. Jentzen, J.-G. Ma, J. A. Shelnutt, Conservation of the conformation of the porphyrin macrocycle in hemoproteins. *Biophys. J.* **74**, 753–763 (1998).
6. X. Ye *et al.*, CO rebinding to protoheme: Investigations of the proximal and distal contributions to the geminate rebinding barrier. *J. Am. Chem. Soc.* **127**, 5854–5861 (2005).
7. T. Kitagawa, Y. Mizutani, Resonance Raman spectra of highly oxidized metalloporphyrins and heme proteins. *Coord. Chem. Rev.* **135–136**, 685–735 (1994).
8. T. Kitagawa, N. Haruta, Y. Mizutani, Time-resolved resonance Raman study on ultrafast structural relaxation and vibrational cooling of photodissociated carbonmonoxymyoglobin. *Biopolymers* **67**, 207–213 (2002).
9. C. Rovira, M. Parrinello, First-principles molecular dynamics simulations of models for the myoglobin active center. *Int. J. Quantum Chem.* **80**, 1172–1180 (2000).
10. A. Arcovito *et al.*, Light-induced relaxation of photolyzed carbonmonoxymyoglobin: A temperature-dependent x-ray absorption near-edge structure (XANES) study. *Biophys. J.* **88**, 2954–2964 (2005).
11. M. Schmidt *et al.*, Ligand migration pathway and protein dynamics in myoglobin: A time-resolved crystallographic study on L29W MbCO. *Proc. Natl. Acad. Sci. U.S.A.* **102**, 11704–11709 (2005).
12. R. M. Esquerra, R. A. Goldbeck, D. B. Kim-Shapiro, D. S. Kliger, Spectroscopic evidence for nanosecond protein relaxation after photodissociation of myoglobin-CO. *Biochemistry* **37**, 17527–17536 (1998).
13. S. E. C. Plunkett *et al.*, Time-resolved step-scan FT-IR spectroscopy of the photodynamics of carbonmonoxymyoglobin. *Appl. Spectrosc.* **49**, 702–708 (1995).
14. D. Kinschel *et al.*, Femtosecond X-ray emission study of the spin cross-over dynamics in haem proteins. *Nat. Commun.* **11**, 4145 (2020).
15. C. Bacellar *et al.*, Spin cascade and doming in ferric hemes: Femtosecond X-ray absorption and X-ray emission studies. *Proc. Natl. Acad. Sci. U.S.A.* **117**, 21914–21920 (2020).
16. J. Kim *et al.*, Anisotropic picosecond X-ray solution scattering from photo-selectively aligned protein molecules. *J. Phys. Chem. Lett.* **2**, 350–356 (2011).
17. M. Levantino *et al.*, Ultrafast myoglobin structural dynamics observed with an X-ray free-electron laser. *Nat. Commun.* **6**, 6772 (2015).
18. F. A. Lima *et al.*, Probing the electronic and geometric structure of ferric and ferrous myoglobins in physiological solutions by Fe K-edge absorption spectroscopy. *Phys. Chem. Chem. Phys.* **16**, 1617–1631 (2014).
19. A. B. Stickrath *et al.*, Detailed transient heme structures of mb-CO in solution after CO dissociation: An X-ray transient absorption spectroscopic study. *J. Phys. Chem. B* **117**, 4705–4712 (2012).
20. W. Zhang *et al.*, Manipulating charge transfer excited state relaxation and spin crossover in iron coordination complexes with ligand substitution. *Chem. Sci. (Camb.)* **8**, 515–523 (2017).
21. M. W. Mara *et al.*, Metalloprotein entatic control of ligand-metal bonds quantified by ultrafast x-ray spectroscopy. *Science* **356**, 1276–1280 (2017).
22. F. Rosca *et al.*, Investigations of anharmonic low-frequency oscillations in heme proteins. *J. Phys. Chem. A* **106**, 3540–3552 (2001).
23. L. V. Dao, R. M. Lowe, W. J. Rowlands, C. N. Lincoln, P. Hannaford, “Three-pulse two-colour photon echo and transient grating studies of myoglobin” in *Femtochemistry and Photobiology*, A. Douhal, S. Jesus, Eds. (World Scientific Publishing, River Edge, NJ, 2002), pp. 815–819.
24. H. S. Cho *et al.*, Protein structural dynamics in solution unveiled via 100-ps time-resolved x-ray scattering. *Proc. Natl. Acad. Sci. U.S.A.* **107**, 7281–7286 (2010).
25. M. Silatani *et al.*, NO binding kinetics in myoglobin investigated by picosecond Fe K-edge absorption spectroscopy. *Proc. Natl. Acad. Sci. U.S.A.* **112**, 12922–12927 (2015).
26. Y. Mizutani, T. Kitagawa, Direct observation of cooling of heme upon photodissociation of carbonmonoxymyoglobin. *Science* **278**, 443–446 (1997).
27. S. G. Kruglik, J.-C. Lambry, J.-L. Martin, M. H. Vos, M. Negre, Sub-picosecond Raman spectrometer for time-resolved studies of structural dynamics in heme proteins. *J. Raman Spectrosc.* **42**, 265–275 (2011).
28. M. Lim, T. A. Jackson, P. A. Anfirud, Femtosecond near-IR absorbance study of photoexcited myoglobin: Dynamics of electronic and thermal relaxation. *J. Phys. Chem.* **100**, 12043–12051 (1996).
29. J. W. Petrich, J. L. Martin, D. Houde, C. Poyart, A. Orszag, Time-resolved Raman spectroscopy with subpicosecond resolution: Vibrational cooling and delocalization of strain energy in photodissociated (carbonmonoxy)hemoglobin. *Biochemistry* **26**, 7914–7923 (1987).
30. J. W. Petrich, C. Poyart, J. L. Martin, Photophysics and reactivity of heme proteins: A femtosecond absorption study of hemoglobin, myoglobin, and protoheme. *Biochemistry* **27**, 4049–4060 (1988).
31. S. Franzen, L. Kiger, C. Poyart, J.-L. Martin, Heme photolysis occurs by ultrafast excited state metal-to-ring charge transfer. *Biophys. J.* **80**, 2372–2385 (2001).
32. X. Ye *et al.*, Investigations of heme protein absorption line shapes, vibrational relaxation, and resonance Raman scattering on ultrafast time scales. *J. Phys. Chem. A* **107**, 8156–8165 (2003).
33. Y. Kholodenko, M. Volk, E. Gooding, R. M. Hochstrasser, Energy dissipation and relaxation processes in deoxy myoglobin after photoexcitation in the Soret region. *Chem. Phys.* **259**, 71–87 (2000).
34. D. Zhu *et al.*, Performance of a beam-multiplexing diamond crystal monochromator at the Linac Coherent Light Source. *Rev. Sci. Instrum.* **85**, 063106 (2014).
35. N. A. Miller *et al.*, Polarized XANES monitors femtosecond structural evolution of photoexcited vitamin B₁₂. *J. Am. Chem. Soc.* **139**, 1894–1899 (2017).

36. L. B. Michocki *et al.*, Probing the excited state of methylcobalamin using polarized time-resolved X-ray absorption spectroscopy. *J. Phys. Chem. B* **123**, 6042–6048 (2019).
37. N. A. Miller *et al.*, Ultrafast X-ray absorption near edge structure reveals ballistic excited state structural dynamics. *J. Phys. Chem. A* **122**, 4963–4971 (2018).
38. N. A. Miller *et al.*, Ultrafast XANES monitors femtosecond sequential structural evolution in photoexcited coenzyme B₁₂. *J. Phys. Chem. B* **124**, 199–209 (2020).
39. S. Della Longa *et al.*, Polarized X-ray absorption spectroscopy of the low-temperature photoproduct of carbonmonoxy-myoglobin. *J. Synchrotron Radiat.* **6**, 1138–1147 (1999).
40. P. Liebisch, H. Dau, Linear dichroism in the XANES of partially oriented samples: Theory and application to the photosynthetic manganese complex. *ChemPhysChem* **11**, 1236–1247 (2010).
41. D. Cabaret, A. Bordage, A. Juhin, M. Arfaoui, E. Gaudry, First-principles calculations of X-ray absorption spectra at the K-edge of 3d transition metals: An electronic structure analysis of the pre-edge. *Phys. Chem. Chem. Phys.* **12**, 5619–5633 (2010).
42. A. Bianconi, M. Dell’Ariccia, A. Gargano, C. R. Natoli, “Bond Length Determination Using XANES” in *EXAFS and Near Edge Structure*, P. A. Bianconi, D. L. Incoccia, D. S. Stipich, Eds. (Springer Berlin Heidelberg, 1983), pp. 57–61.
43. S. A. Wilson *et al.*, X-ray absorption spectroscopic investigation of the electronic structure differences in solution and crystalline oxyhemoglobin. *Proc. Natl. Acad. Sci. U.S.A.* **110**, 16333–16338 (2013).
44. T. E. Westre *et al.*, A multiplet analysis of Fe K-edge 1s → 3d pre-edge features of iron complexes. *J. Am. Chem. Soc.* **119**, 6297–6314 (1997).
45. B. D. Dunietz, A. Dreuw, M. Head-Gordon, Initial steps of the photodissociation of the CO ligated heme group. *J. Phys. Chem. B* **107**, 5623–5629 (2003).
46. M. Levantino *et al.*, Observing heme doming in myoglobin with femtosecond X-ray absorption spectroscopy. *Struct. Dyn.* **2**, 041713 (2015).
47. L. U. Brinkmann, J. S. Hub, Ultrafast anisotropic protein quake propagation after CO photodissociation in myoglobin. *Proc. Natl. Acad. Sci. U.S.A.* **113**, 10565–10570 (2016).